GFZ
Helmholtz-Zentrum
POTSDAM

Originally published as:

Kronberg, E. A., Rashev, M. V., Daly, P. W., Shprits, Y., Turner, D. L., Drozdov, A., Dobynde, M., Kellerman, A. C., Fritz, T. A., Pierrard, V., Borremans, K., Klecker, B., Friedel, R. (2016 online): Contamination in electron observations of the silicon detector onboard Cluster/RAPID/IES instrument in Earth's radiation belts and ring current. - *Space Weather*, *14*, 6, pp. 449—462.

DOI: http://doi.org/10.1002/2016SW001369

AGU PUBLICATIONS

Space Weather

RESEARCH ARTICLE
10.1002/2016SW001369

Key Points:
- IES data in the radiation belts contaminated by energetic protons and electrons
- Radiation belt regions and energies of contamination are identified
- Methods to correct the IES data are proposed

Correspondence to:
E. A. Kronberg,
kronberg@mps.mpg.de

Citation:
Kronberg, E. A., et al. (2016), Contamination in electron observations of the silicon detector onboard Cluster/RAPID/IES instrument in Earth's radiation belts and ring current, *Space Weather*, *14*, 449–462, doi:10.1002/2016SW001369.

Received 19 JAN 2016
Accepted 3 JUN 2016
Accepted article online 10 JUN 2016
Published online 29 JUN 2016

©2016. The Authors.
This is an open access article under the terms of the Creative Commons Attribution-NonCommercial-NoDerivs License, which permits use and distribution in any medium, provided the original work is properly cited, the use is non-commercial and no modifications or adaptations are made.

Contamination in electron observations of the silicon detector on board Cluster/RAPID/IES instrument in Earth's radiation belts and ring current

E. A. Kronberg[1,2], M. V. Rashev[1], P. W. Daly[1], Y. Y. Shprits[3,4,5], D. L. Turner[6], A. Drozdov[3], M. Dobynde[7], A. C. Kellerman[3], T. A. Fritz[8], V. Pierrard[1,9,10], K. Borremans[9], B. Klecker[1,11], and R. Friedel[1,2,12]

[1]Max Planck Institute for Solar System Research, Göttingen, Germany, [2]Ludwig Maximilians University, Munich, Germany, [3]Department of Earth Planetary and Space Sciences, University of California, Los Angeles, California, USA, [4]Department of Earth Atmospheric and Planetary Sciences, Massachusetts Institute of Technology, Cambridge, Massachusetts, USA, [5]Helmholtz Centre Potsdam GFZ German Research Centre for Geosciences and University of Potsdam, Potsdam, Germany, [6]The Aerospace Corporation, El Segundo, California, USA, [7]Skolkovo Institute of Science and Technology, Skolkovo, Russia, [8]Center for Space Physics, Boston University, Boston, Massachusettes, USA, [9]Belgian Institute for Space Aeronomy, Brussels, Belgium, [10]TECLIM, Earth and Life Institute, Université Catholique de Louvain, Louvain-La-Neuve, Belgium, [11]Max Planck Institute for extraterrestrial Physics, Garching, Germany, [12]Space Science and Applications, Los Alamos National Laboratory, Los Alamos, New Mexico, USA

Abstract Since more than 15 years, the Cluster mission passes through Earth's radiation belts at least once every 2 days for several hours, measuring the electron intensity at energies from 30 to 400 keV. These data have previously been considered not usable due to contamination caused by penetrating energetic particles (protons at >100 keV and electrons at >400 keV). In this study, we assess the level of distortion of energetic electron spectra from the Research with Adaptive Particle Imaging Detector (RAPID)/Imaging Electron Spectrometer (IES) detector, determining the efficiency of its shielding. We base our assessment on the analysis of experimental data and a radiation transport code (Geant4). In simulations, we use the incident particle energy distribution of the AE9/AP9 radiation belt models. We identify the Roederer L values, $L^\star$, and energy channels that should be used with caution: at $3 \leq L^\star \leq 4$, all energy channels (40–400 keV) are contaminated by protons (≃230 to 630 keV and >600 MeV); at $L^\star \simeq 1$ and 4–6, the energy channels at 95–400 keV are contaminated by high-energy electrons (>400 keV). Comparison of the data with electron and proton observations from RBSP/MagEIS indicates that the subtraction of proton fluxes at energies ≃ 230–630 keV from the IES electron data adequately removes the proton contamination. We demonstrate the usefulness of the corrected data for scientific applications.

1. Introduction

Monitoring and predicting the Earth's radiation environment is extremely important in the context of space weather [e.g., *Kessel et al.*, 2013]. There are many different spacecraft which provide energetic particle observations in the radiation belts [e.g., *Lazaro et al.*, 2014]. However, it is known that in this hazardous region it is quite a challenge to obtain pure, caveat-free particle data [e.g., *Friedel et al.*, 2005]. The energetic particles in the Earth's space environment, in spite of careful instrument protection, produce erroneous signals in the particle detectors by penetrating through the shielding. Additionally, it is important to know the characteristics of the detector material as it imposes limits on the energy range of particles which can be reliably measured [e.g., *Carron*, 2006].

The Cluster mission [*Escoubet et al.*, 1997] has been surveying the terrestrial space environment with four satellites for more than 15 years. During its polar trajectory it provides snapshots of the different parts of the Earth's radiation belts once per orbit, now covering more than one solar cycle. The Research with Adaptive Particle Imaging Detector (RAPID) on board Cluster [see *Wilken et al.*, 2001] measures energetic electrons and ions, providing the scientific community with a vast amount of particle data in the radiation belts.

One of the most important issues in space weather model development is the quality of the input data [*Vainio et al.*, 2009]. Unfortunately, the electron RAPID measurements, designed for the range of 30–400 keV and for operation in regions outside the radiation belts, can be contaminated by protons and electrons with much

higher energies (protons at >100 keV and electrons at >400 keV) from the space environment. This is a major issue especially in the radiation belts. For example, another particle instrument on board Cluster, the Cluster Ion Spectrometry with the time-of-flight ion mass spectrometer, also suffers from penetrating radiation which has been carefully corrected for [*Mouikis et al.*, 2014].

In this study we assess a possible contamination of the data from the RAPID/IES silicon detector by energetic protons and electrons and we evaluate the data quality. Using Geant4 [*Agostinelli et al.*, 2003; *Allison et al.*, 2006], we model the instrument geometric configuration and evaluate its response to an incident flux of protons and electrons in a wide energy range.

We evaluate the performance of the IES instrument in three steps. First, we assess the deposition energy of the 40 keV–8 MeV electrons and 100 keV–400 MeV protons in the silicon detector using experimental data. Second, we model a planar geometry of IES in Geant4 and compare deposition energy obtained from the modeling and the experimental data. In the third step, we build a detailed geometry of IES in Geant4, introduce distributions of incoming electrons/protons according to the AE9/AE9 radiation belt models [*Ginet et al.*, 2013], and calculate contaminations by electrons and protons.

In section 2, we describe instrumentation and data used for the study. The energy deposition of electrons and protons in the silicon detectors without any shielding are calculated using experimental data in section 3. In section 4, using Geant4 modeling, we assess the contamination of the IES detector, first without shielding to verify simulations, and then with shielding, as in reality. We compare our results with data from the Van Allen Probes (also referred to as Radiation Belt Storm Probes, RBSP) Magnetic Electron Ion Spectrometer (MagEIS) [*Blake et al.*, 2013]. Applications are presented in section 6. A summary of the results is in section 7.

The results of this study demonstrate the capabilities of this silicon detector in the radiation belt environment and beyond. They help to identify and correct contaminated electron observations. We also show that the RAPID/IES data obtained in the radiation belts which previously were considered rather unusable can be utilized in particular cases.

2. Instrumentation and Data

The Cluster mission consists of four identical spacecraft flying in a tetrahedron-like formation. It was launched in 16 July 2000. The Cluster spacecraft follow an elliptical polar orbit with a period of 57 h (lately reduced to 54 h). Initially, the perigee of the highly elliptical orbit was at $\simeq 4\ R_E$ (i.e., inside the radiation belts at $L \simeq 4$; the typical location of the radiation belts can be found in *Ganushkina et al.* [2011]) and the apogee was at $\simeq 19 R_E$. The orbit of the spacecraft evolves with time. The perigees reduced to a few 100 km ($L < 1$) in 2011 and then started to rise again reaching $L \simeq 5$ in 2016. The orbital plane has rotated away from a 90° inclination. More information about the Cluster mission and instrumentation is given in *Escoubet et al.* [1997].

The RAPID instrument consists of two different and independent systems for the detection of the electrons and ions: the Imaging Electron Spectrometer (IES) and the Imaging Ion Mass Spectrometer (IIMS) [*Wilken et al.*, 1997]. Both instruments cover 180° in polar angle, and by utilizing the spacecraft spin (with period 4 s), they provide the distribution of particles with complete coverage of the unit sphere in phase space. We will study the response of the IES detector to the radiation belt environment, and we will assess model predictions of proton contamination in electron data using IIMS ion measurements.

The IES detector measures electrons with energies from ~30 keV to ~ 400 keV. The definition of the six electron energy channels is shown in Table 1. The image plane of three acceptances "pinhole" systems is formed by an advanced microstrip solid state detector with a planar format 0.5 cm × 1.5 cm and three individual elements, see Figure 1. Therefore, each system divides an acceptance angle of 60° in three angular intervals. An energy loss < 400 keV will be classified as an electron, although it could be due to penetrating particles as discussed later.

IIMS consists of three identical detector heads and uses a combination of time of flight and energy measurements to classify and bin the incident particles. In this study we use proton data which are measured in the energy range from 28 keV to 4 MeV. The seven proton energy channels are shown in Table 1. The IIMS instrument is also sensitive to penetrating particles, but it does not count them because of time-of-flight filtering. In general, the particle detector may be affected by several events at the same time: a real event and an event produced by a penetrating particle. These pileup effects can be controlled using RAPID/SGL product [see *Kronberg and Daly*, 2015]. The time resolution of the RAPID omnidirectional data is one spin (~4 s).

Table 1. Lower Thresholds of Energy Channels for Electrons and Protons for RAPID

Channel	Electrons (keV)	Protons (keV)
1	39.2	28–64[a]
2	50.5	75
3	68.1	92
4	94.5	160
5	127.5	374
6	244.1	962
7	—	1885
Upper	406.5	4007

[a]Energy gap between hydrogen 1 and 2.

To cross check our results, we use RBSP/MagEIS observations. The two RBSP probes were launched in August 2012 into near-equatorial orbit, with apogees at $L \simeq 6$ and perigees at $L \simeq 700$ km. The MagEIS particle spectrometers on each spacecraft measure electrons at energies from ≃20 keV to 4.8 MeV and protons from ≃55 keV to 20 MeV [*Blake et al.*, 2013]. These are nominal energy ranges only, and the exact range can vary. In this study we use RBSP-A, *L* shell-sorted, Level 2 data with removed background [*Claudepierre et al.*, 2015].

3. Energy Loss of Electrons and Protons in the IES Silicon Detector: Verification With Experimental Data

First, the energy loss of electrons and protons in the IES silicon detector can be calculated using experimental data from the National Institute of Standards and Technology (NIST) and the Stopping and Range of Ions in Matter (SRIM) program for calculating the interaction of ions in matter. The results for the particle energy deposits in a silicon detector with a thickness of 800 μm without shielding are shown in Figure 2. The results for calculations with NIST tables show that electrons above 400 keV can deposit energy less than 400 keV in the detector (see Figure 2, left) and, therefore, be detected erroneously. Protons at energies below 10 MeV will deposit all their energy in the IES detector (see Figure 2, right). Additionally, protons at energies >600 MeV can be detected as electrons, as energy deposition of such protons is less than 400 keV (see Figure 2, right).

Thus, this quick evaluation shows that the IES detector can be contaminated by both the high-energy electrons and protons. In the following, we assess the contamination of the IES detector using Geant4 simulations.

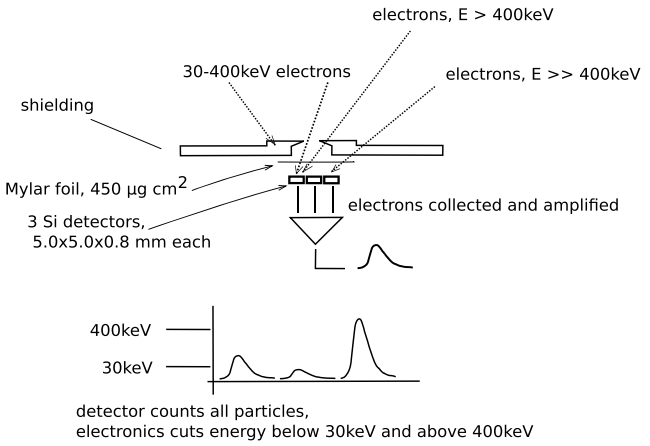

Figure 1. Working principle of one of the three IES heads, which contains three solid state detectors shielded in front by foil. The dashed lines show trajectories of penetrating electrons at different energies. The two dotted lines for 30–400 keV electrons indicate that at this energy range, the particles reach the detectors only through the open entrance. The dashed line for electrons with energies ≫400 keV shows that those particles reach the detectors by penetrating the structures. Electrons with energies >400 keV can penetrate the thin part of the structure but not the thick parts.

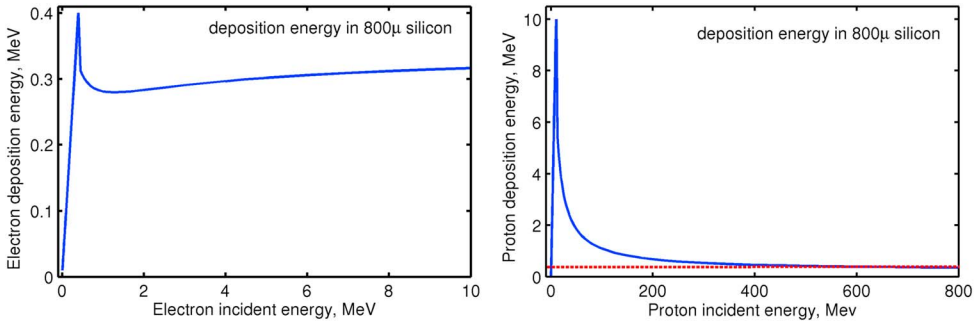

Figure 2. Deposition energy on the IES silicon detector of (left) electrons and (right) protons up to 800 MeV calculated from the NIST tables. Red dashed line shows that protons at energies >600 MeV will deposit energy less than 400 keV on silicon detector.

These simulations are closer to reality because they include the shielding of the silicon detectors and the supporting construction elements. Moreover, the energy deposition in instrument materials by energetic particles is modeled in greater detail.

4. Simulations in Geant4

We conduct two types of simulations: (1) silicon detector without shielding and (2) silicon detector with shielding using the actual IES geometry with cover and support plates made of aluminum. The simulation without shielding allows us to cross check the simulations with experimental data (NIST tables) shown in section 3.

Geant4 simulations enable us to use a complex geometry (large number of shapes and materials) and to simulate in a statistical manner the interaction between an impactor and a target. In general, the geometry significantly modifies the signal-to-noise ratio which is important for interpreting the measurements.

4.1. Simulations Without Shielding

In section 3 we considered only a silicon detector of 800 μm thickness. Here we add the foil (see Figure 1) and the dead layer. The thickness of the Mylar foil in front of the detector is about 2 μm and the dead layer is considered to be less than 1 μm. The detector was bombarded by particle fluxes that were isotropic and uniform in energy. The results of the silicon detector simulations without any shielding are shown in Figure 3. Because of the complexity of the physics underlying electron interaction with matter [e.g., *Fichtner*, 1985], Monte Carlo methods are used in Geant4 simulations to calculate the energy deposition. The electron energy deposition shows significant scatter. Each point in Figure 3 results from electron paths through the matter. Each of the electron trajectories are quite different. However, the average red line in Figure 3 agrees well with a statistically averaged curve from the experimental results from NIST tables in Figure 2. It shows that electrons above 400 keV are detected as having an energy near 400 keV. For protons, which are heavier and propagate rather straight [e.g., *Tavernier*, 2010], the deposition energy curves show the same linear slope in the range up to 10 MeV (Figure 3 shows only energies up to 2 MeV). This gives us confidence in our Geant4 simulations. The foil and the dead layer included in Geant4 simulations produce an additional difference. That is, protons

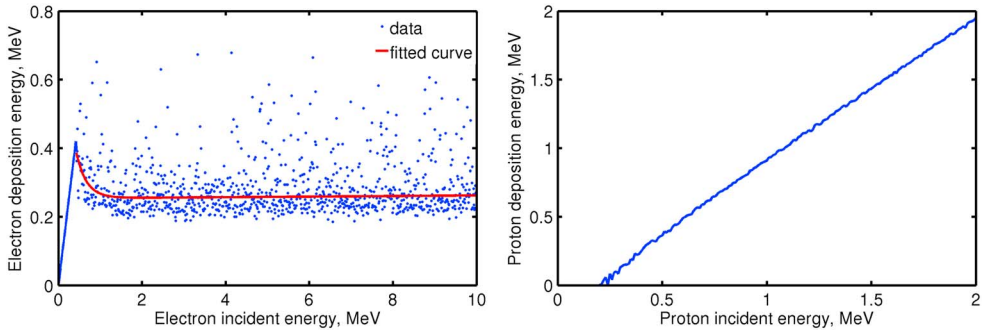

Figure 3. Deposition energy on the IES detector, without shielding, from (left) electrons and (right) protons, as simulated by Geant4. Note the different ranges of incident energy for electrons and protons.

lose ~200 keV of their energy when passing through the foil and the dead layer. This is reflected by a vertical shift of the proton deposition energy by ~200 keV in Figure 3 (right).

4.1.1. Results: Contamination by Electrons

The results of the simulations show that the electrons above 400 keV can deposit energy less than 400 keV in the detector, see Figure 3 (left) and therefore, be detected erroneously. These energetic electrons are counted mainly in the highest IES energy channels 5 and 6 (Table 1). The working principles of the silicon detector assume that the intensity (or differential particle flux) of electrons significantly decreases with an increase of particle energy. Thus, the effect of contamination by high-energy electrons would be negligible. However, this depends on the hardness of the energy spectrum. We consider that energetic electrons are counted in the last IES energy channel 6 (244–406 keV). When the electron energy spectral index γ, ($I_e \sim E^{-\gamma}$, where I_e is the electron intensity and E is the particle energy) is harder than 4 ($\gamma < 4$), the contamination will be larger than 10% (the precision of RAPID/IES data). Considering that high-energy electrons are counted in the fifth energy channel (128–244 keV), the critical value of γ will be ~2.7. Otherwise, the high-energy electron contamination is insignificant, less than 1%.

4.1.2. Results: Contamination by Protons

As mentioned in section 4.1, the incoming energy of protons is first reduced by ~200 keV due to interaction with the foil and the dead layer in front of the detector. The foil in front of the detector, the dead layer, and the electronic noise define the lowest energy which can be measured. For the IES detector, the lowest detection limit is about ~30 keV. Thus, protons should have at least about ~230 keV in order to be registered by the IES detector. The results derived by NIST tables and our Geant4 simulations indicate that protons at energies up to 10 MeV deposit all their energy in the IES detector, see Figure 2 (right). However, the onboard electronics will cut off all signals above 400 keV and will subsequently determine the upper energy limit. Only protons with energies from ~230 to ~630 keV can be detected as electrons. Protons at energies higher than ~630 keV will be detected as having energies higher than ≃400 keV (~630 keV – 230 keV = 400 keV) and will be cut off by the electronics. Additionally, protons at energies >600 MeV can be detected as electrons, as mentioned in section 3.

4.2. Simulations with Shielding

We implement a detailed geometry of the IES instrument in the Geant4 environment including all parts which are meant to shield high-energy electrons and protons: aluminum shielding, Mylar foil, and supporting structures. The assembled IES sensor in Geant4 environment can be seen in Figure 4. Due to geometrical symmetry, we model 1/4 of the entire 4π space. Therefore, we use two out of three identical IES sensors.

We bombard the given model with electrons and protons in the *Y*-*Z* plane (see Figure 4), changing the incident angle from 0° to 90° with a step of 1°. The energy distribution of incoming particles is derived from the AE9 and AP9 radiation belt models (version 1.20.002). We used the mean values of omnidirectional differential particle fluxes for $1 \leq L^* \leq 9$, with L^* being the Roederer L value for the quiet external magnetic field model from Olson-Pfitzer [*Roederer*, 1970; *Olson and Pfitzer*, 1977]. The energies ranged from 40 keV to 8 MeV for electrons and from 100 keV to 400 MeV for the protons. The values are calculated in the equatorial plane over all magnetic local times. The input spectra are shown in Figure 5.

In these simulations we do not bombard the model from all possible directions in 3-D space. Our 2-D model represents the worst case in which the incident particles are directed such that many of them enter through the open entrance of the detector (see Figure 4). Some of these produce spurious measurements. If we add a third dimension, the erroneously measured particles will be mainly those which penetrate the detector shielding from the *X* direction (see Figure 4). Such a penetration through the shielding is also possible in the 2-D model, however. The thickness of the shielding is not significantly different in the third (*X*) direction compared to the thickness in *Y* and *Z*. The 2-D model is thus viable as a first approximation. We note that the Geant4 model follows the radiation response only. The electrical signal formation in the detector and the electronics that actually produces the measurement signal and the associated caveats are not considered here.

4.2.1. Results: Electrons and Protons

The results of the simulations which present the contamination percentage of the RAPID/IES energy channels at different $L^\star$ are shown in Figure 6 and their values can be found in Table 2.

The percentage of contamination by protons at $3 \leq L^\star \leq 4$ is very high. This area corresponds to the slot region in the electron radiation belts. The electron intensities are therefore relatively low compared to proton intensities in the proton radiation belt. We trust the first three channels at $1 \leq L^\star \leq 2$ and $L^\star \simeq 6$. This means

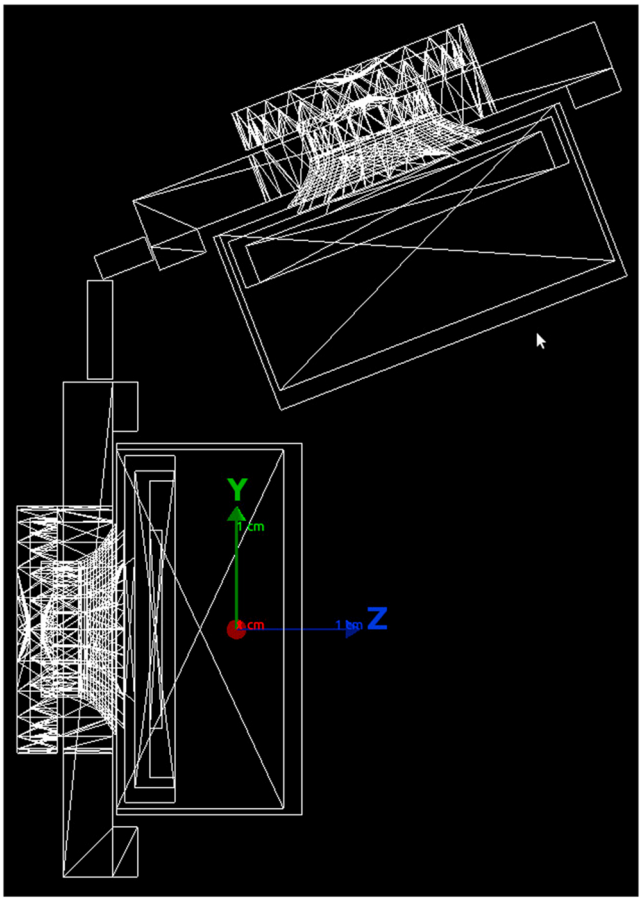

Figure 4. Two IES sensor heads constructed in Geant4 environment.

that the contamination is less than 10% which is on the order of the RAPID/IES measurement precision. For $7 \leq L^{\star} \leq 9$ we trust the first four channels while channels 5 and 6 tend to be contaminated.

These results assume an average radiation environment derived from AE9/AP9 models. They do not take into account specific temporal variations of the radiation belts.

5. Comparison with RBSP/MagEIS Observations

We compare electron observations RAPID/IES (244–407 keV) with electron observations by RBSP/MagEIS (234–317 keV) in 2012, day of year (DOY) 245–366. At this time, the IES electron sensors were still only mildly degraded [*Kronberg and Daly*, 2015]. In Figure 7, we show the uncorrected electron IES data (Figure 7a),

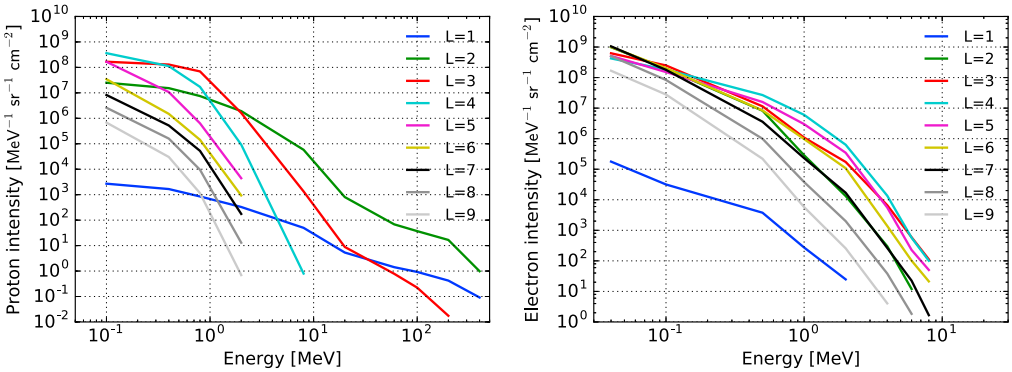

Figure 5. Differential particle fluxes for (left) protons and (right) electrons versus energy for different values of L^{*}.

Table 2. Contamination (%) of the IES Detector in the Earth's Radiation Belts

	Contamination (%)					
Channel	1	2	3	4	5	6
			L^*=1			
Electrons	1.03	3.28	7.27	25.85	35.43	34.89
Protons	1.6	4.23	5.02	5.2	6.04	8.62
Total	2.63	7.51	12.29	31.06	41.47	43.51
			L^*=2			
Electrons	0.32	1.02	2.35	10.8	20.06	22.2
Protons	2.55	6.93	9.68	12.88	17.04	24.33
Total	2.87	7.95	12.04	23.68	37.1	46.53
			L^*=3			
Electrons	0.62	1.23	2.97	11.04	13.83	11.28
Protons	18.97	31.73	40.21	46.6	54.9	66.65
Total	19.59	32.96	43.18	57.64	68.73	77.93
			L^*=4			
Electrons	2.38	4.31	14.92	32.25	35.42	30.3
Protons	29.03	36.77	33.78	28.41	28.96	34.49
Total	31.41	41.08	48.7	60.66	64.38	64.79
			L^*=5			
Electrons	1.76	4.32	11.02	35.96	42.65	40.94
Protons	7.51	10.77	9.18	6.2	5.29	5.47
Total	9.27	15.09	20.2	42.16	47.94	46.41
			L^*=6			
Electrons	0.5	1.66	4.65	20.19	30.33	33.41
Protons	0.83	1.58	1.5	1.26	1.12	1.14
Total	1.33	3.24	6.15	21.44	31.45	34.55
			L^*=7			
Electrons	0.18	0.69	1.99	10.59	21.01	27.01
Protons	0.26	0.61	0.69	0.75	0.8	0.93
Total	0.44	1.3	2.68	11.34	21.81	27.94
			L^*=8			
Electrons	0.09	0.38	1.09	6.45	15.79	22.93
Protons	0.17	0.42	0.52	0.62	0.73	1.64
Total	0.26	0.8	1.61	7.07	16.53	24.57
			L^*=9			
Electrons	0.06	0.25	0.72	4.48	12.8	20.67
Protons	0.11	0.27	0.34	0.42	0.51	0.63
Total	0.17	0.52	1.06	4.9	13.31	21.3

RBSP-A/MagEIS electron data (Figure 7b), and their ratio (Figure 7c) from September to December 2012. The median values of spin-averaged fluxes are collected in bins of 1 DOY × 0.1*L*. We use the MagEIS data to validate our contamination coefficients derived with Geant4 simulations (section 4.2.1).

The comparison shows that the IES data have a smaller signal-to-noise ratio. This is well seen in the region between the *L* shells 3 and 4 during DOY 330–365 (Figures 7a and 7b). There the background electron intensities observed by RAPID are between ≃100 and 1000 keV^{-1} sr^{-1} cm^{-2} s^{-1}, where background intensities of MagEIS (Figure 7b) are less than 100 keV^{-1} sr^{-1} cm^{-2} s^{-1}. During events, (e.g., the electron injection around DOY 352, see Figure 7b), intensity enhancements are very pronounced in MagEIS data (≃10^4 keV^{-1} sr^{-1} cm^{-2} s^{-1}) but are quite faint in the RAPID observations (≃$2 \cdot 10^3$ keV^{-1} sr^{-1} cm^{-2} s^{-1}). The validation of the contamination

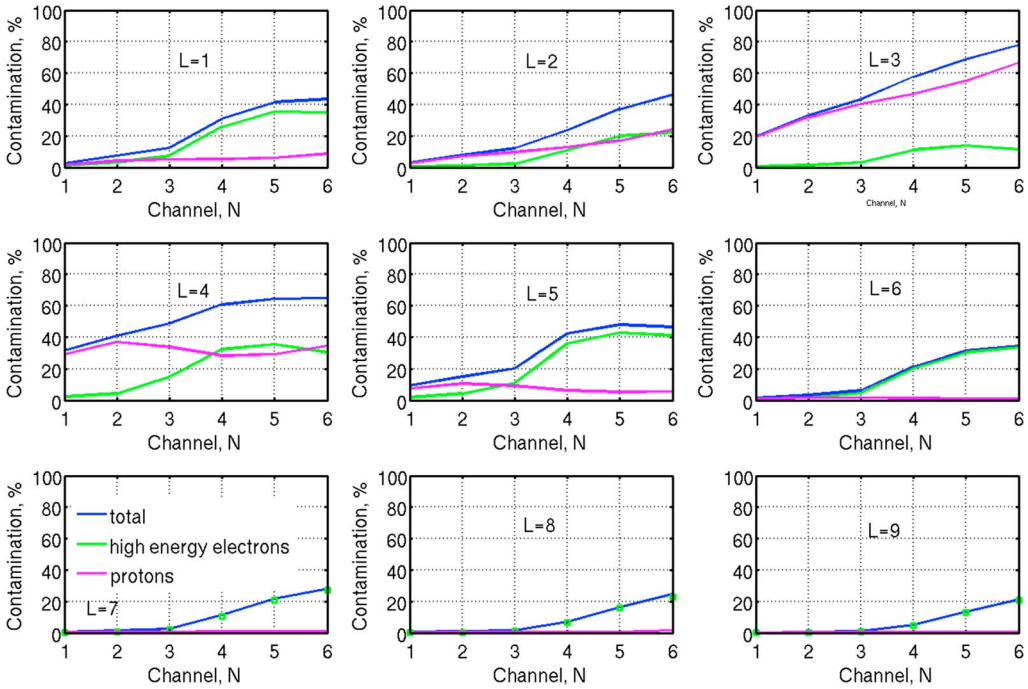

Figure 6. IES data contamination in the electron and proton radiation belts at different L^* shells, for different energy channels and for the solar maximum. The percentage of the contamination by protons, high-energy electrons, and the sum of those is denoted by magenta, green, and blue colors, respectively.

coefficients is complicated because IES data have additional problems to be considered. The data suffer from (1) background noise which is presumably caused by cosmic rays, see *Kronberg and Daly* [2015]; and (2) the electron sensor degradation since 2007, see *Kronberg and Daly* [2015]. Also, two instruments may not have the same absolute values of electron intensities due to different measurement and calibration techniques. We model these effects with the function

$$\log_{10} X' = b \log_{10}(X \circ M) - a; X' = (X \circ M)^b / 10^a, \tag{1}$$

where X' is the corrected IES electron data and X is the uncorrected IES data. We choose to work with logarithms of the intensities because they range by 4 orders of magnitude. Moreover, this ansatz takes into account that the energy spectra at these energies often follow an exponential function [e.g., *Cayton et al.*, 1989]. M is the correction matrix for electron and proton contamination derived with Geant4 simulations whose values shown in Table 2. $\circ$ denotes the Hadamard (element-wise) product. The parameter b corrects for sensor degradation and the parameter a removes background noise. These two parameters show the best fit when one uses logarithms of the intensities. The differences in the instrumentation of the spacecraft and calibration are contained in the parameters a and b. We find the parameters a and b by minimizing the difference between RBSP-A and corrected Cluster observations,

$$\text{median}\left\{\log_{10} Y - \left[b \log_{10}(X \circ M) - a\right]\right\}^2, \tag{2}$$

where Y is the MagEIS electron data. For the optimization we use differential evolution, as implemented in the SciPy software package, to find the values a and b for which the expression in equation (2) is minimal. The best fit is obtained with the values 2.1 and 1.6 for a and b. Therefore, the corrected IES electron data are $X' \simeq (X \circ M)^{1.6}/100$ (method I, see Figure 7d). The corrected data agrees much better with the MagEIS data, see the ratios of the IES (uncorrected/corrected) to MagEIS electron intensities in Figures 7c and 7f, respectively. The median ratio value before the correction is 3.1, after the correction it is 0.86.

We can use the proton observations of RBSP-A/MagEIS to prove that protons 230–630 keV contaminate the IES electron observations, see Figure 7e. For this we subtract the proton intensities measured by RBSP-A from the electron intensities instead of using proton contamination coefficients from Table 2. For this we minimize the function

$$\text{median}\left\{\log_{10} Y - \left[b \log_{10}(X \circ M' - cP) - a\right]\right\}^2, \tag{3}$$

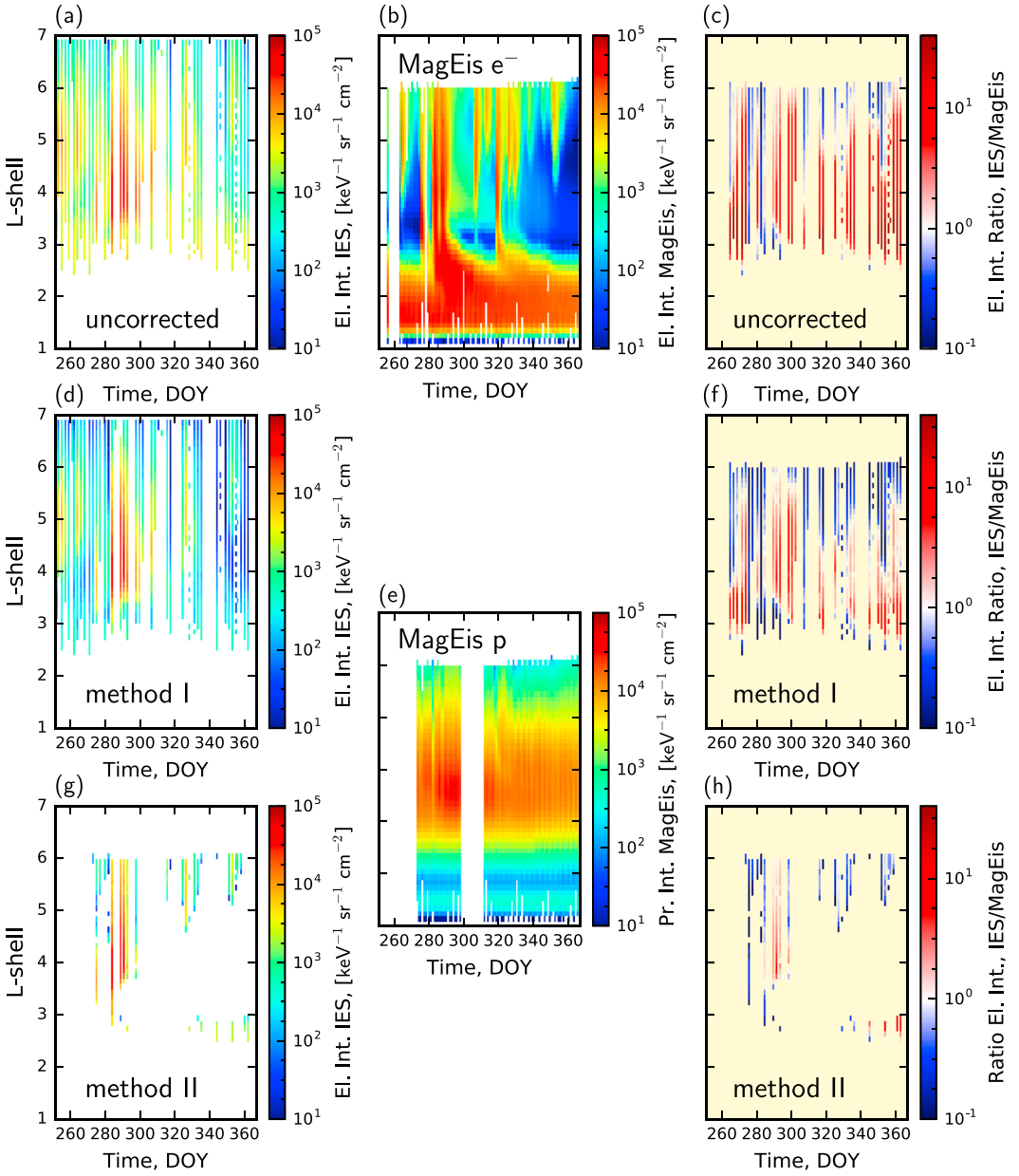

Figure 7. Time evolution of IES electron intensities at 244 to 407 keV: (a) uncorrected and (d) corrected using contamination coefficients derived with Geant4 simulations, see Table 2 and (g) corrected by subtracting the MagEIS proton intensities at energies predicted by Geant4 simulations , Figure 7e; (b and e) MagEIS electron (234–317 keV) and proton (229–636 keV) intensities; and the ratio of IES to MagEIS electron intensities: (c) IES uncorrected, (f) IES corrected by method I and (h) IES corrected by method II; versus *L* shell from September to December 2012. The *L* shell is calculated using a dipolar field. The white color in Figures 7a and 7b and 7d and 7e and 7g) and the yellow color in Figures 7c and 7f indicate that there are no meaningful electron/proton observations.

where M' is the electron contamination derived by Geant4 observations, c is an optimization parameter, and P are the proton intensities observed by the RBSP-A/MagEIS instrument at energies from 229 to 636 keV. The best fit is obtained with $a \simeq 0$, $b \simeq 1$, and c in the range from 0.55 to 1. This implies that the background contamination represented by parameter a and the effect imposed by the sensor degradation are relatively small in the radiation belt observations and proportional to the proton intensities.

The level of degradation of the electron sensor can be induced by the nonionizing energy loss of the protons in the silicon detectors, especially at energies on the order of hundreds of keV [*Summers et al.*, 1993]. Therefore, we expect a correlation between the proton intensity and the level of damage. According to Geant4

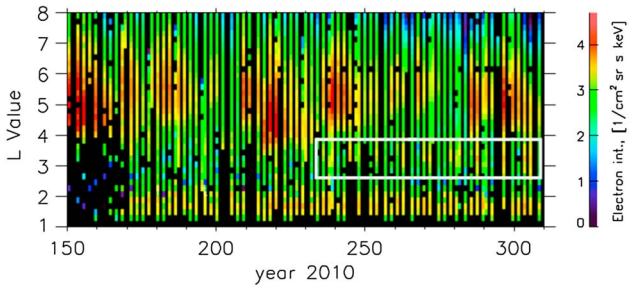

Figure 8. Uncorrected intensities of electrons at energies from 240 to 400 keV versus *L* shell and time for DOY 150 to 310 2010. White dashed line shows the "third radiation belt" structure.

simulations, the contamination by electrons (M') does not lead to substantial changes in the electron intensity. The IES electron observations are mostly contaminated by protons at energies from ≃230 to 630 keV. The subtraction of proton intensities measured by MagEIS from the uncorrected data leads to electron observations with similar injection features as those from MagEIS, see Figure 7g compared to Figure 7b. The ratio between the corrected IES and MagEIS electron intensities (from Figures 7g and 7b, respectively) is ≃0.55 (see Figure 7h) which is reasonable considering that the spacecraft are at different locations. The RBSP-A mainly covered local times (LTs) from ∼0 to 12, while Cluster covered LT from ∼0 to 18. The covered magnetic latitudes are not the same: RBSP-A has a rather equatorial orbit and the Cluster satellites fly at higher latitudes due to polar orbiting.

Therefore, the subtraction of proton fluxes at ≃230 to 630 keV from the electron data can be used as an alternative method (II) for liberating data from proton contamination.

Both these methods, (I) and (II), lead to improved IES electron data in the radiation belts. The correction method (I) based on the coefficients from the simulations is weaker. For example, it may not subtract the radiation belt contamination between approximately DOY 285 and 300 at $L \simeq 4$, see Figure 7d. This is removed by the second method which subtracts the simultaneously observed proton intensities. It is impossible to reproduce all dynamical features using an averaged model of the radiation belts.

6. Application to the Radiation Belts

6.1. Third Radiation Belt

To illustrate the usefulness of these results, we show how the contamination can be misinterpreted. The RAPID/IES electron data seem to indicate the existence of an additional radiation belt at a distance of 3 to ∼3.5 R_E at low electron energies, observable at time scales of many months for several years (2010–2012). In Figure 8, we plot electron observations (channel 6) by the RAPID/IES on all Cluster spacecraft in the radiation belts for the days 150–310 in 2010 versus *L* shell (at different magnetic latitudes). The alleged third radiation belt is highlighted by the white dashed line. The following contamination analysis shows that it is an artifact.

The results from the Geant4 simulations show that at approximately $L = 3$, the data are extremely contaminated by the protons. If we remove the relative contamination of the protons from the electron observations

$$I_{e,\,clean} = I_e - CI_e, \tag{4}$$

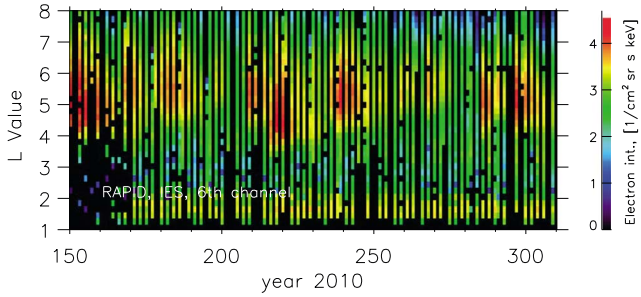

Figure 9. Intensities of electrons at energies from 240 to 400 keV versus *L* shell and time for DOY 150 to 310 2010 after applying cleaning procedure.

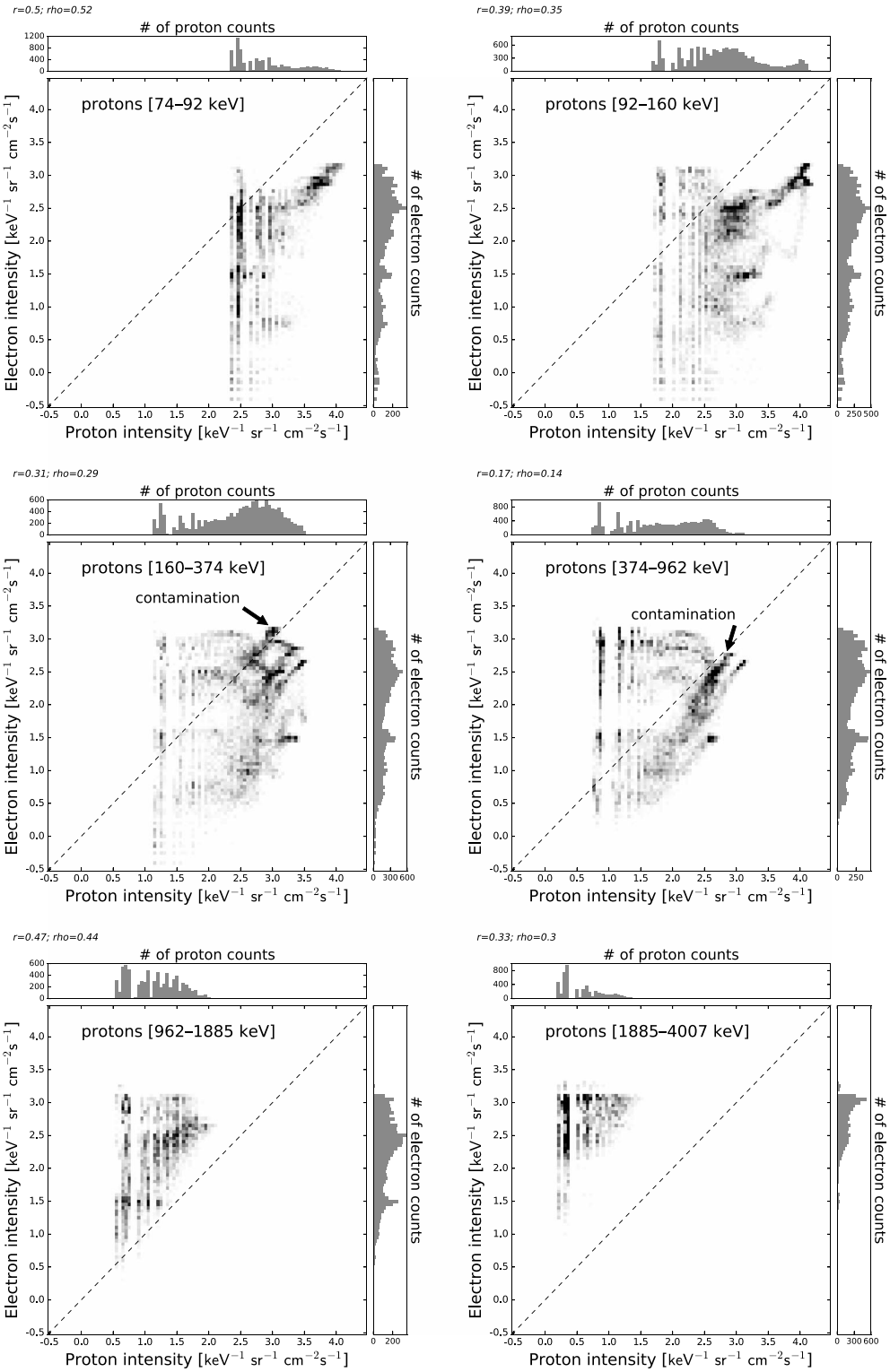

Figure 10. Electron intensity at 240–400 keV (channel 6) versus proton intensity measured by RAPID/IIMS for the energy channels (top left) at 74–92 keV (channel 2), (top right) at 92–160 keV (channel 3), (middle left) at 160–374 keV (channel 4), (middle right) at 374–962 keV (channel 5), (bottom left) at 962–1885 keV (channel 6), and (bottom right) at 1885–4007 keV (channel 7). The observations are from 2010 (0–≃119 and ≃169–184 DOY), at $2.2 < L < 3.5$. The data are collected in 100 bins for both electrons and protons. The color indicates the number of points in each bin (increasing from white to black). One-dimesional histograms have been added at the top and the right of each plot, showing the sum in the respective direction of the 2-D plot. The dashed line indicates equal proton and electron counts.

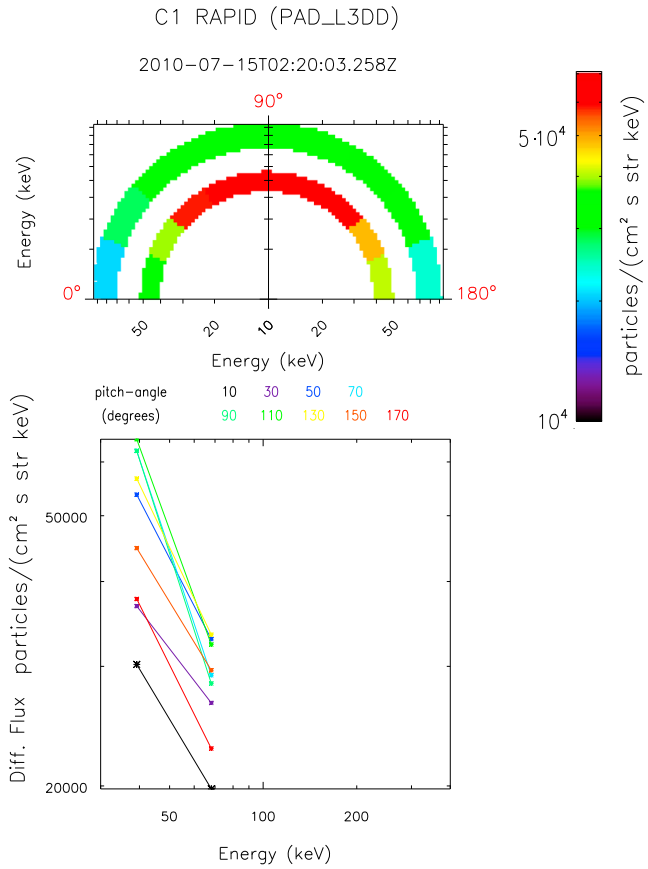

Figure 11. Equatorial distribution functions of a typical chorus event observed on 15 July 2010 on board Cluster C1 at L≃5. (top) The electron wheel plot (distribution of pitch angle as a function of energy for two channels) measured by RAPID/IES instrument. (bottom) The electron differential fluxes (the different pitch angle ranges are color coded) as a function of energy observed during this event. The observed values are used to compute the electron distribution functions in the model. Adapted from *Breuillard et al.* [2015].

where C is the contamination percentage taken from Table 2, we will see that the third radiation belt has disappeared (see Figure 9). Here we assume that the range of proton energies that cause this contamination (230 to 630 keV) are well represented by the AP9 fluxes during this time. The proton belts typically are relatively stable in the inner region. Those data, however, are still fairly contaminated by the high-energy electrons (in the range from about 11% at $L^\star \simeq 3$ to about 41% at $L^\star \simeq 5$, see Table 2). Therefore, this plot can reveal details about the electron flux dynamics at energies ≥240 keV in the radiation belts. It should be noted that this is not an integral flux ≥240 keV, as some of the electrons at energies <400 keV may erroneously be detected in other electron channels.

In order to confirm the proton contamination, we plot observations of electron versus proton intensities at six different energy ranges for $L \simeq 3$ (see Figure 10). In these plots, the data at low electron intensities ($< 10^2$ keV^{-1} sr^{-1} cm^{-2} s^{-1}, say) are attributed to background. For sufficiently high electron intensities, we expect to observe a linear correlation between electrons (240–400 keV, channel 6) and protons at energies from ~230 to ~630 keV (see section 4.1.2). In particular, such a correlation is expected for intensities of electrons higher than the background ($\simeq 10^2$ keV^{-1} sr^{-1} cm^{-2} s^{-1}). This electron population produces "the alleged faint third radiation belt" in the time interval ≃169–184 DOY in Figure 8 (for the other time intervals shown in the plot, proton observations were not available). Electrons at high intensities $> 10^2$ keV^{-1} sr^{-1} cm^{-2} s^{-1} are well correlated with the protons with intensities $> 10^2$ keV^{-1} sr^{-1} cm^{-2} s^{-1} in channels 4 and 5 (160–374 and 374–962 keV), see Figure 10 (middle row). A high number of measurements with near-equal proton and electron count (dashed line) is likely caused by contamination. Protons at these energy channels approximately lie within the predicted contamination energy range from (230 to 630 keV). We do not observe such a correlation between the electron intensities and those from protons at energies 74–92 and 92–160 keV (Figure 10,

top row) as well as at 962–1885 and 2885–4007 keV (Figure 10, bottom row). This confirms the predictions of the Geant4 simulations.

6.2. Using IES Data in the Radiation Belts and Ring Current Studies

There are also positive examples. For example, *Breuillard et al.* [2015], in their analysis of the chorus waves, used RAPID/IES observations at $L \simeq 5$ for channels 1 and 3 and studied the electron anisotropy along the magnetic field. Channel 2 is omitted because 3-D electron distributions in the nominal mode are available only in channels 1 and 3 [*Daly and Kronberg*, 2010]. The derived anisotropy was then used as input for their numerical model. The electron anisotropy was calculated using a pitch angle distribution along the magnetic field (see Figure 11). Both plots indicate that the distribution peaks at about 90°. The results in Table 2 show that the data in channel 1 is possibly contaminated by protons at a level of ~8% and by high-energy electrons at a level of ~1.8%. This is the order of precision of RAPID/IES measurements. Therefore, in this case, the RAPID/IES data can be used. In channel 3, the contamination is ~11% and ~9%, respectively. This means that 20% of the electron data are contaminated. Therefore, this energy channel should not be used in the calculations of the input parameters. Also, the spectral slope shown in Figure 11 has some uncertainty due to the ~20% contamination implied by Table 2. If the higher-energy channels (4–6) would be available/used, they would likely suffer from > 40% contamination.

7. Conclusions

The electron data measured by the RAPID/IES detector in the radiation belts must be treated carefully. At all energy channels (40–400 keV), the data are strongly contaminated by protons with ≃230 to 630 keV and >600 MeV at $3 \leq L^{\star} \leq 4$. Furthermore, the highest IES energy channels (95–400 keV) are suffering from contamination by high-energy electrons (>400 keV) at $L^{\star} \simeq 1, 4-6$. However, choosing carefully the energy channels and the L shells according to the results of Geant4 simulations (Table 2), one can still use the IES radiation belt and ring current observations. The contamination can be neglected in cases in which it is less than ≃10% because this is the precision level of RAPID/IES measurements precision.

The results of this study can be used to correct the data in contaminated regions. (1) In case of simultaneous availability of electron intensities and proton intensities in the range from ≃200 to 630 keV, we recommend to subtract the proton intensities from the electron intensities as described in section 5. (2) In case that proton intensities in the aforementioned range are not available, we recommend to use equation (4) and the corresponding coefficients in Table 2 to remove the proton and electron contaminations. This increases the value of RAPID/IES data for scientific investigations, in particular regarding the ring current and the radiation belts of Earth.

Acknowledgments

We would like to thank Chris Perry and Patrick Cruce for useful discussions. We acknowledge the Deutsches Zentrum für Luft und Raumfahrt (DLR) for supporting the RAPID instrument at MPS under grant 50 OC 1401. The Cluster data can be found at CSA Archive: http://www.cosmos.esa.int/web/csa/. We acknowledge RBSP ECT team for the MagEIS data. They can be found at http://www.rbsp-ect.lanl.gov/. The NIST tables are available at http://physics.nist.gov/PhysRefData/Star/Text/ESTAR.html. The SRIM software was taken from http://www.srim.org/#SRIM. The AE9/AP9/SPM software is provided under the link https://www.vdl.afrl.af.mil/programs/ae9ap9. For calculations we used SciPy software package version 0.16.1 available at http://www.scipy.org/.

References

Agostinelli, S., et al. (2003), Geant4 a simulation toolkit, *Nucl. Instrum. Methods Phys. Res., Sect. A*, *506*(3), 250–303, doi:10.1016/S0168-9002(03)01368-8.

Allison, J., et al. (2006), Geant4 developments and applications, *IEEE Trans. Nucl. Sci.*, *53*(1), 270–278, doi:10.1109/TNS.2006.869826.

Blake, J. B., et al. (2013), The Magnetic Electron Ion Spectrometer (MagEIS) Instruments Aboard the Radiation Belt Storm Probes (RBSP) spacecraft, *Space Sci. Rev.*, *179*, 383–421, doi:10.1007/s11214-013-9991-8.

Breuillard, H., et al. (2015), Field-aligned chorus wave spectral power in Earth's outer radiation belt, *Ann. Geophys.*, *33*, 583–597, doi:10.5194/angeo-33-583-2015.

Carron, N. J. (2006), *An Introduction to the Passage of Energetic Particles Through Matter*, pp. 171–301, CRC Press, Boca Raton, Fla.

Cayton, T. E., R. D. Belian, S. P. Gary, T. A. Fritz, and D. N. Baker (1989), Energetic electron components at geosynchronous orbit, *Geophys. Res. Lett.*, *16*, 147–150, doi:10.1029/GL016i002p00147.

Claudepierre, S. G., et al. (2015), A background correction algorithm for Van Allen Probes MagEIS electron flux measurements, *J. Geophys. Res. Space Physics*, *120*, 5703–5727, doi:10.1002/2015JA021171.

Daly, P. W., and E. A. Kronberg (2010), RAPID products at the cluster active archive, *Geosci. Instrum. Methods Data Syst.*, *3*, 41–48, doi:10.1007/978-90-481-3499-1_9.

Escoubet, C. P., R. Schmidt, and M. L. Goldstein (1997), Cluster-Science and mission overview, *Space Sci. Rev.*, *79*, 11–32.

Fichtner, W. (1985), Physics of VLSI processing and process simulation, in *Silicon Integrated Circuits, Applied Solid State Science: Supplement 2, Part C*, edited by D. Kahng, pp. 119–325, Academic Press, Orlando, Fla.

Friedel, R. H. W., S. Bourdarie, and T. E. Cayton (2005), Intercalibration of magnetospheric energetic electron data, *Space Weather*, *3*, S09B04, doi:10.1029/2005SW000153.

Ganushkina, N. Y., I. Dandouras, Y. Y. Shprits, and J. Cao (2011), Locations of boundaries of outer and inner radiation belts as observed by Cluster and Double Star, *J. Geophys. Res.*, *116*, A09234, doi:10.1029/2010JA016376.

Ginet, G. P., et al. (2013), AE9, AP9 and SPM: New models for specifying the trapped energetic particle and space plasma environment, *Space Sci. Rev.*, *179*, 579–615, doi:10.1007/s11214-013-9964-y.

Kessel, R. L., N. J. Fox, and M. Weiss (2013), The Radiation Belt Storm Probes (RBSP) and space weather, *Space Sci. Rev.*, *179*, 531–543, doi:10.1007/s11214-012-9953-6.

Kronberg, E. A., and P. W. Daly (2015), Calibration report of the RAPID measurements in the Cluster Active Archive (CAA), Tech. Rep. CAA-EST-CR-RAP, European Space Agency, Paris.

Lazaro, D., D. Boscher, S. Bourdarie, A. Sicard-Piet, G. Rolland, R. Ecoffet, and E. Lorfevre (2014), Radiation belt activity indices and solar proton event alarm, *IEEE Trans. Nucl. Sci.*, *61*, 1671–1678, doi:10.1109/TNS.2013.2296115.

Mouikis, C. G., L. M. Kistler, G. Wang, and Y. Liu (2014), Background subtraction for the Cluster/CODIF plasma ion mass spectrometer, *Geosci. Instrum. Methods Data Syst.*, *3*, 41–48, doi:10.5194/gi-3-41-2014.

Olson, W. P., and K. A. Pfitzer (1977), Magnetospheric magnetic field modeling, Annu. Sci. Rep. Contract F44620-75-C-0033, Air Force Off. of Sci. Res., McDonnell Douglas Astronautics Co., Huntington Beach, Calif.

Roederer, J. G. (1970), *Dynamics of Geomagnetically Trapped Radiation*, Springer, New York.

Summers, G. P., E. A. Burke, P. Shapiro, S. R. Messenger, and R. J. Walters (1993), Damage correlations in semiconductors exposed to gamma, electron and proton radiations, *IEEE Trans. Nucl. Sci.*, *40*, 1372–1379, doi:10.1109/23.273529.

Tavernier, S. (2010), Interactions of particles in matter, in *Experimental Techniques in Nuclear and Particle Physics*, edited by S. Tavernier, pp. 23–53, Springer, Berlin., doi:10.1007/978-3-642-00829-0

Vainio, R., et al. (2009), Dynamics of the Earth's particle radiation environment, *Space Sci. Rev.*, *147*, 187–231, doi:10.1007/s11214-009-9496-7.

Wilken, B., et al. (1997), RAPID—The imaging energetic particle spectrometer on Cluster, *Space Sci. Rev.*, *79*, 399–473, doi:10.1023/A:1004994202296.

Wilken, B., et al. (2001), First results from the RAPID imaging energetic particle spectrometer on board Cluster, *Ann. Geophys.*, *19*, 1355–1366.